Monthly Notices of the ROYAL ASTRONOMICAL SOCIETY

MNRAS **525,** 3541–3550 (2023) https://doi.org/10.1093/mnras/stad2536
Advance Access publication 2023 August 31

Intelligent monitoring and diagnosis of telescope image quality

Tianzhu Hu [1,2] Yong Zhang [1,3]★ Jiaqi Yan,[4] Ou Liu,[5] Huaiqing Wang[1,2] and Xiangqun Cui[1,2]

[1]*National Astronomical Observatories/Nanjing Institute of Astronomical Optics & Technology, Chinese Academy of Science, Nanjing 210042, China*
[2]*CAS Key Laboratory of Astronomical Optics & Technology, Nanjing Institute of Astronomical Optics & Technology, Nanjing 210042, China*
[3]*National Astronomical Observatories, Chinese Academy of Sciences, Beijing 10049, China*
[4]*School of Information Management, Nanjing University, Nanjing 210023, China*
[5]*Wenzhou Institute, University of Chinese Academy of Sciences, Zhejiang 325001, China*

Accepted 2023 August 17. Received 2023 August 8; in original form 2023 March 29

ABSTRACT

The imaging quality of a telescope directly affects the reliability of astronomical research. Through the monitoring and diagnosis of imaging quality, the cause of the deterioration of imaging quality can be found in time, which is essential for ensuring the peaking performance of the telescope and high-quality imaging. Moreover, these operations are complex and crucial for achieving high-quality imaging of future giant telescope systems involving active optics, adaptive optics, and other advanced techniques. We propose a three-component method based on cutting-edge artificial intelligence technology to real-time monitor and efficiently diagnose the telescope image quality. The first component, an image quality monitoring system, monitors and outputs the telescope's image quality. The second component is a query system with a knowledge graph, which outputs the node chains as the possible cause of poor image quality based on the input. The third component, a final estimator, uses the node parameter, which contains historical fault data and real-time updated data from sensors, to give the probability of each node chain. We construct and test the system in the Large Sky Area Multi-Object Fiber Spectroscopy Telescope.

Key words: methods: data analysis – methods: numerical – techniques: image processing – software: data analysis.

1 INTRODUCTION

Imaging data is one of the essential products of the telescope and provides valuable scientific research information. The imaging quality directly affects the reliability of the research results. Many observatories spend considerable time and money to enhance and optimize the imaging quality of their telescopes, for example, by enlarging the aperture of telescopes, operating adaptive optics techniques, launching the telescope into space, and installing higher resolution cameras.

However, the telescope may be unable to image at optimal quality because of atmospheric parameters, improper operation, and device fault. Several methods have been proposed to maintain the peaking performance of the telescope and ensure high-quality imaging. The Sloan Digital Sky Survey telescope (McGehee et al. 2002; Gunn et al. 2006) and the Very Large Telescope (Shanks et al. 2015) mount many sensors to monitor telescope devices and atmospheric parameters, which will warn the maintainers when engineering parameters approach the threshold values. Using a large amount of logbook data, the LIGO observatory constructs an information retrieval and recommendation system (Abbott et al. 2009; Mukund et al. 2018) based on the natural language process technology to speed-up the discovery of historical fault information. The Australian Radio Telescope (Landau 1994) and *Hubble Space Telescope* (Burrows et al. 1991; Gerb 1991) build fault tree-based expert systems for fault diagnosis to improve maintenance efficiency.

The causes of poor imaging quality are complicated, as advanced technologies and devices are applied to future giant telescopes, such as active, adaptive optics technology, and interferometer. The current method keeps high-quality imaging by efficient fault diagnosis and critical parameter monitoring. These methods need the maintainer to set the thresh value and transfer fault performance to the phrase used for the query, which relies on the maintainer's experience. Artificial intelligence technology is widely used for data analysis and decision support (Gómez et al. 2019; Longo, Merényi & Tiňo 2019) to simplify manual operations and improve the efficiency of operations. Proposing an intelligent monitoring and diagnosis method for the telescope image quality is necessary.

Teimoorinia et al. (2020) use combined machine-learning models to classify the image quality; Hu et al. (2021) achieve telescope image quality monitoring and classification and give the possible cause of poor image quality. This paper aims to provide an interpretable diagnosis method of image quality with high-efficiency according to the classification results of the image quality. The telescope is a system composed of many complex units, among which telescope devices, site environment, and human factors affect the image quality. The most challenging task in image quality diagnosis is finding the cause according to the limited information. Knowledge graphs (KGs) have shown exemplary performance in expressing the complex relationship and reasoning the result by limited information (Chen, Jia & Xiang 2020; Hogan et al. 2021). For example, KGs have been used in improving search capabilities (Zou 2020), providing user recommendations (Guo et al. 2022; Xie et al. 2021), facilitating research and discovery (Xu et al. 2020), and assessing and mitigating risk (Tissot & Pedebos 2021).

★ E-mail: yzh@niaot.ac.cn

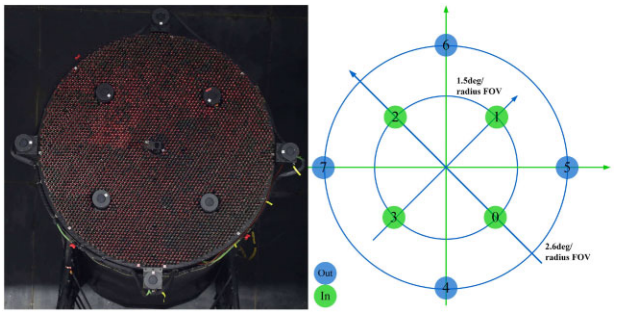

Figure 1. The focal surface of LAMOST and the positions of the acquisition cameras. The left image shows the focal surface, which is mounted with eight 2048 × 2048 pixels cameras; the right image shows the relative positions of eight cameras, four inner cameras in the 3-degree FOV in green and four outer cameras in the 5.2-degree FOV in blue.

Figure 2. Three types of relationship of different entities.

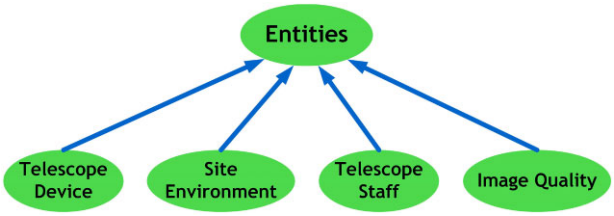

Figure 3. Classes of telescope entities.

We propose a three-component telescope image quality monitoring and diagnosis system (IQMDS) to meet future giant telescopes' high-image quality needs. The first component, an image quality monitoring system (IQMS), monitors the telescope image quality and transfers the star image to a core phrase of image quality. The second component, a query system based on the KG, can find out the possible cause of poor image quality in the form of node chains. The third component is a final estimator, which combines historical data and real-time high-frequency data from sensors to give the probability of each node chain. This method uses artificial intelligence technology to replace manual monitoring and diagnosis of telescope image quality, helping to increase data output and keep image quality.

This paper provides an approach accessible for most telescopes, although it uses the Large Sky Area Multi-Object Fabre Spectroscopic Telescope (LAMOST) (Cui et al. 2012; Zhao et al. 2012) as an example for illustration. Eight acquisition cameras are mounted across the LAMOST focal surface, shown in Fig. 1. We use the star image captured by the acquisition camera as the system's input for monitoring and diagnosing image quality.

The paper is organized as follows. Section 2 briefly introduces the KG technology and the telescope image quality KG. We present the detail of the telescope image quality monitoring and diagnosis in Section 3. A telescope IQMDS based on LAMOST is introduced and analysed in Section 4. Finally, we give the conclusion in Section 5.

2 KNOWLEDGE GRAPHS

Singhal (2012) first proposed the KG used in the searching machine in 2012. KGs describe the relationship between different entities, which contains much prior knowledge. KGs can mine, organize, and effectively manage knowledge from large-scale data to improve the information process's quality and efficiency and provide users with more intelligent services. This part introduces the KGs representation method, related entities of telescope image quality, and their relationship.

2.1 NEO4J

There are two types of KG data models: resource description framework (RDF) (Manola et al. 2004) graphs and attribute graphs. RDF is a standard directed data model for presenting information on the web. RDF is a triple fact (Subject–Predicate–Object). The core structure of attribute graphs is a set of triple (head entity, relationship, and tail entity), and every entity can add the attribute. Entities are connected through connections to form a net-like structure. NEO4J is an attribute graph data base focusing on data structures, data model features, and query facilities. Because adding and refreshing node properties are necessary for telescope maintenance KGs, our established KG and query system are based on NEO4J.

2.2 Concept layer of knowledge graph

Top-down or bottom-up methods could be used to construct a KG. The top-down approach has two steps: firstly, the concept layer needs to be built by the expert, and then the instance extracted from an amount of operational data is added to the KG. This paper builds the concept layer of KG based on the expert experiment and maintenance logbook. To help the understanding of the graph, we arranged some arrow rules shown in Fig. 2.

The telescope image quality KG needs to contain the telescope image quality and all the entities that may affect the image quality. Entities can be classified into four classes, i.e. image quality, telescope device, telescope staff, and site environment in the telescope image quality domain. The classes of telescope entities are shown in Fig. 3.

The different classes have different properties, which can help optimize the image quality and estimate the cause of the fault. The four classes of entities are defined below.

Definition 1: Telescope device

A telescope device entity has three properties, represented by a triple $td = <s, l, n>$, where s is a list of special properties of the telescope device which can be detected by the sensor, for example, the force value of a force actuator or the thickness of an oil pad. The l and n represent the label (the device category) and the device's name, respectively.

Definition 2: Telescope image quality

A telescope image quality entity has one property n, which is the name of telescope image quality.

Definition 3: Staff

A staff entity has two properties and is represented by a couple $st = <n, o>$, where n is the role name of the staff, and o is an operation of the staff role.

Definition 4: Environment

An environment entity has two properties and is represented by a couple $e = <s, n>$, where s is a list of the special properties of the environment, for example, wind speed and temperature value; n is the name of the environment.

Figure 4. The telescope device contains the optics system, dome and support building, structure, control system, and terminal instrument.

Some triples (head entity, relationship, and tail entity) connect each other to construct an event; *s* and *o* are essential for evaluating whether the event is established.

The telescope device is pivotal for monitoring and diagnosing imaging quality. Any fault in the telescope device can directly impact the imaging quality, and skilled operators can enhance the image quality through adept operation of the equipment. Fig. 4 gives the telescope device classification base on the classification criteria of the report of KECK (Nelson, Mast & Faber 1985), SALT (Stobie, Meiring & Buckley 2000), E-ELT (Tamai & Spyromilio 2014), and LAMOST (Cui et al. 2012). Telescope devices are classified into optics systems, dome and support buildings, structures, control systems, and terminal instruments, and every sub-class contains many entities.

2.3 The relationship of different class

The telescope monitoring and diagnosis KG describes the relationships between different entities, which include those connecting image quality with the telescope device, image quality with the site environment, and telescope device with person factor. The telescope device and site environment affect the image quality directly, while telescope staff affects the telescope image quality by affecting the telescope device or doom environment. We introduce these below, respectively.

We take LAMOST as an example to introduce the relationship between these four classes of entities. Because of the inevitable influence on LAMOST from atmospheric turbulence and long-time exposure imaging, each acquisition camera obtains circular star images with Gaussian image intensity profiles. The telescope's image quality deteriorates, and its state manifests as the image spot size becomes larger and the image spot shape deviates from the circle.

We analysed these relationships using the maintenance logbook, daily observation status reports, expert experiments, and optics software simulation. The maintenance logbook records the telescope faults, the description of the faults and the fault reasons; The daily observation status report records the device sensor parameters, atmospheric seeing, weather, wind speed, and temperature.

2.3.1 Relationship between image quality and telescope device

The relationship between the telescope device and image quality is shown in Fig. 5. The telescope device contains the optics system, dome and support building, structure, control system, and terminal instrument. Image quality is present by star image shape and size.

The terminal instrument will generate a pure black picture if the dome is not opened. The telescope sub-mirror tilt will cause a two-point-like star image; poor performance of active optics will cause a lumpy-like star image; telescope structure shaking and poor performance of tracking-pointing control system will lead to a stick-like star image; and telescope focal surface defocusing will lead to a donut-like star image. Focal surface defocuses and active optics errors will make the star image larger, while tilt or defocus of the terminal instrument will lead to a donut-like star image.

2.3.2 Relationship between image quality and site environment

The site environment influences the telescope image quality, and astronomers always spend much time on site selection. According to the site selection research report and weather station data (Aksaker et al. 2020; Deng et al. 2021), we divided the site environment parameters into elevation, climatic condition, atmospheric seeing, luminosity of night sky, atmospheric extinction, and atmospheric scattering.

All site environment parameters affect the telescope image quality. The bright night sky will cause dim stars in the picture. Climate condition mainly contains temperature T, pressure P, and humidity RH. These parameters affect the atmospheric index n and satisfy the following:

$$n = 1 + 7.86 \times \frac{10^{-4} P}{273 + T} - 1.5 \times 10^{-11} RH \left(T^2 + 160\right). \quad (1)$$

The uneven distribution of the refractive index on the optical path can lead to poor seeing. Therefore, rapid changes in these climate parameters can cause poor seeing, resulting in large size star images. Strong wind speed can also rapidly change the temperature and pressure and even cause telescope structure shaking, leading to a stick-like star image. It must be mentioned that ventilation and refrigeration systems can adjust the temperature to improve the image quality. The detail is shown in Fig. 6.

2.3.3 Relationship between staff and other entities

Telescope operation and maintenance need a lot of staff, including astronomers, maintainers, and operators. Astronomers set the observation strategy of the telescope and guide the operator and maintainer; operators are responsible for the control system, dome and support building on–off; and maintainers maintain the telescope before and after operating the telescope.

If operators do not adhere to the standard operating procedures during device usage, it can lead to irregularities or even device malfunctions. The lack of proper operation of the refrigeration and ventilation systems before observation prevented the reduction of the temperature difference between the dome's interior and exterior, resulting in poor dome seeing and consequently leading to a larger star image. Failing to select the appropriate reference star hindered the active optics system's capacity to accurately calibrate the mirror surface, consequently producing a lumpy-like star image. Further details are illustrated in Fig. 7.

And the site environment also affects the telescope staff's work; for example, high elevation leads to the lack of oxygen, which increases the work difficulty of the maintainers and operators.

3 TELESCOPE IMAGE QUALITY MONITORING AND DIAGNOSIS SYSTEM

Telescope IQMDS contains an IQMS, a KG result generation system (KRGS) and a final estimator. The shape classification based on

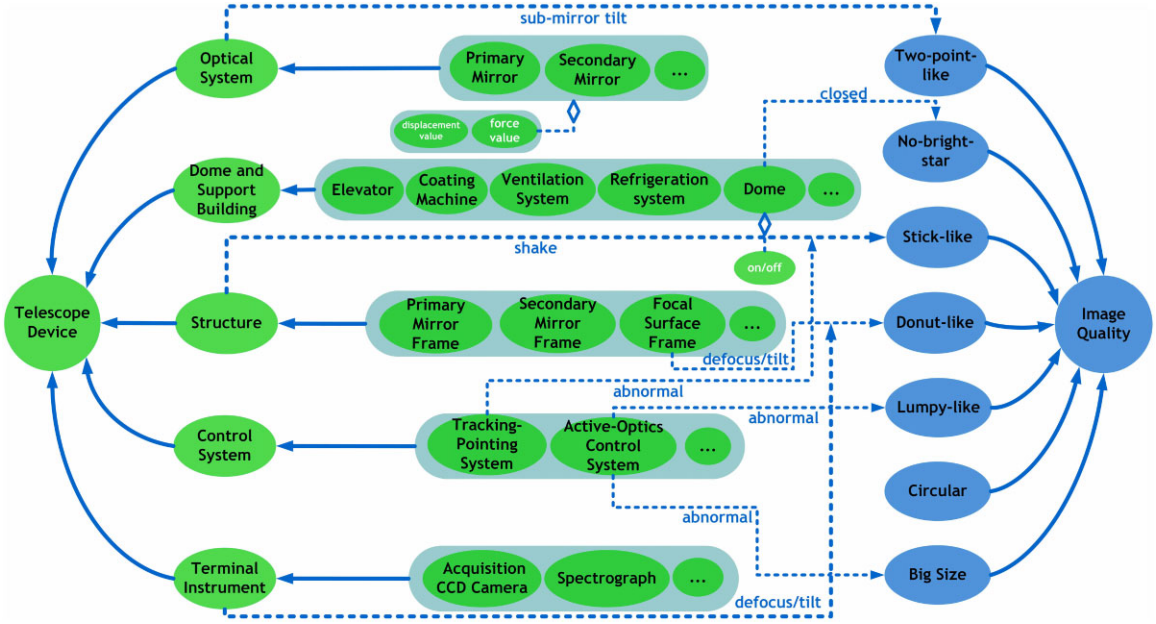

Figure 5. Relationships between telescope devices and image quality.

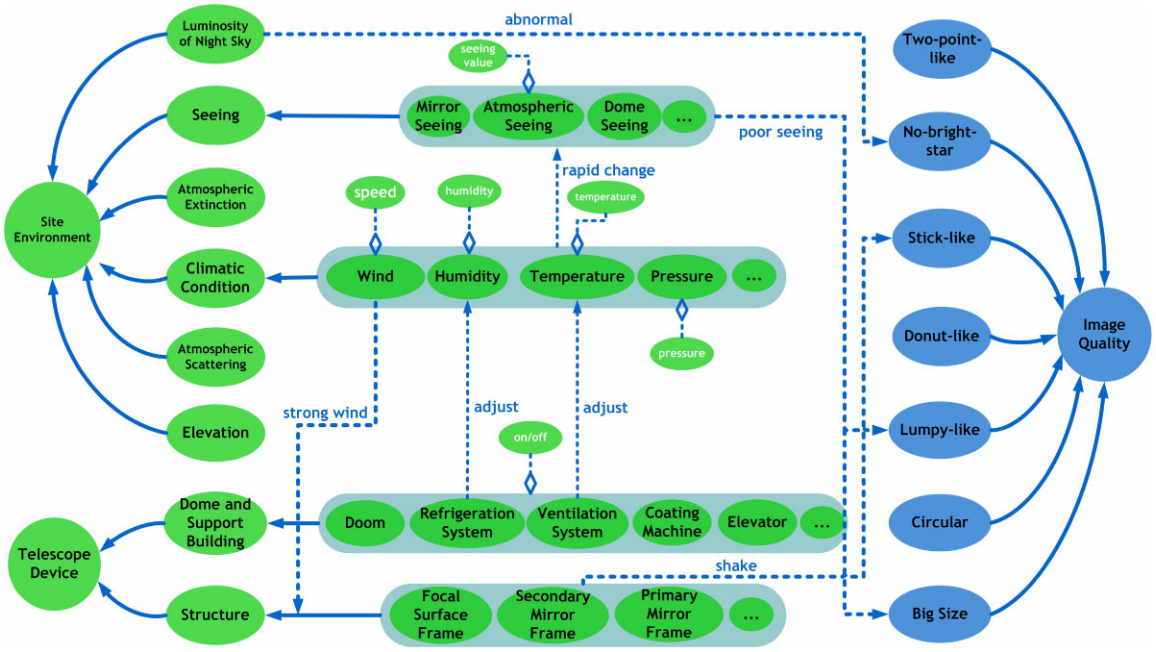

Figure 6. Relationship between image quality and site environment.

machine learning and the corresponding relationship of star shape with image quality is the core of the IQMDS. The KG is the core of the KRGS system based on the rich expert experience. In this part, we take LAMOST as an example to introduce our method.

3.1 Image Quality Monitoring System

A well-experienced maintainer can quickly determine the cause of the poor image quality based on the star image. Because there is a relationship between the star image shape and image quality, we can use the star image shape and size to represent the telescope image quality.

The monitoring system needs to divide the normal and abnormal star images to monitor the image quality. Convolutional neural networks (CNN) (Lawrence et al. 1997; Zheng et al. 2020) have excellent performance in classification tasks. CNN mainly includes convolution, pooling, and fully connected layers and uses the convolution kernel of the convolutional layer to extract image features. After multiple convolutional layers, the data is transmitted to the fully connected neural network (FNN) and the softmax layer for classification.

The monitoring system takes two steps. First, we use picture features and the random forest algorithm (RF) to select normal pictures captured by the acquisition camera or science camera; then,

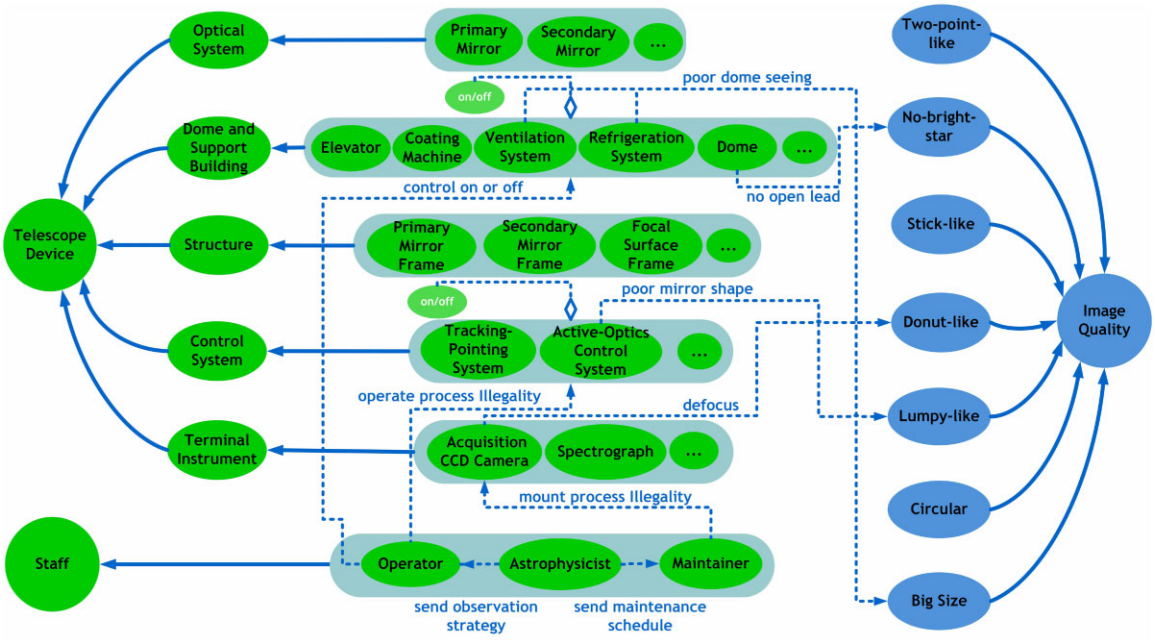

Figure 7. Relationship between image quality and staff.

we cut out and extract the single star image from the source image of the picture (Hu et al. 2021). The star image size is measured by the full width at half-maximum, and CNN classifies the star image shape. Details of the algorithm are given in Algorithm 1.

Algorithm 1 Star image shape classification.

Require:
Science camera or acquisition camera picture, pic;
Trained RF construct, RF;
Trained CNN construct, CNN;
Ensure: Star image shape, s;
Import the pic to RF, judge whether has bright star in picture;
if No bright star is true **then**
    s is no bright star
else
    Cut out the star image from pic;
    Import the star image to CNN;
State CNN output the s;
end if
return s;

The star shape is divided into five according to the CNN classification; when the shape of the star image deviates from the circle or the size of the star image is too large, the monitoring system warns the maintainer and feeds the image quality to the second component.

3.2 Knowledge graph result generation system

Telescope image quality KG contains the whole relationship of image-quality-related entities and gives interpretable causes of changes in the shape and size of telescope star images. According to the core phrase of telescope image quality extracted by the IQMS, the KRGS can generate the sub-KGs by the below steps:

(1) Use the input core phrase to query in the KG-based query system to obtain the node A_0 with the core phrase as the name.

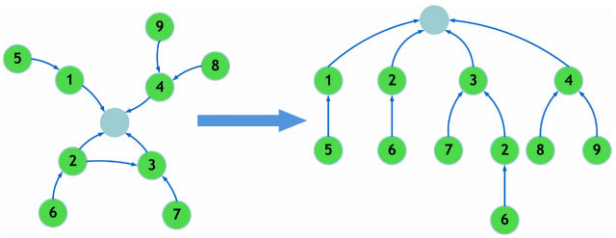

Figure 8. Sub-KGs transfer to node chains.

(2) Nodes set S, which point to the A_0, is got;
(3) Find the all nodes which point to nodes contain in set S as new nodes set;
(4) Repeat step (2) and (3) until they cannot find the new node.

We can find the initial node, which no other nodes point to in the KG subgraph, and get the path from the initial node to the imaging quality node. This process is shown in Fig. 8; the nodes on the path and relationships between the nodes construct the node chains. A node chain represents an event that includes causality, and all node chains are fed to the final estimator. The detail of the KRGS based on LAMOST is provided in sub-section 4.2.

3.3 Final Estimator

KRGS can find out the possible cause of poor telescope image quality, but it is necessary to give the probability of each reason for efficient diagnosis. In this part, we use the node parameter, which contains historical fault data and real-time updated data from sensors, to give the probability of each node chain. We assume that the more times a certain fault causes this type of imaging quality in history, the greater the probability that this type of image quality will be driven by it again.

Tuple (head entity, relationship, and end entity) describes an action, and some tuples construct node chains. The probability of a node chain being the cause of poor imaging quality can be expressed

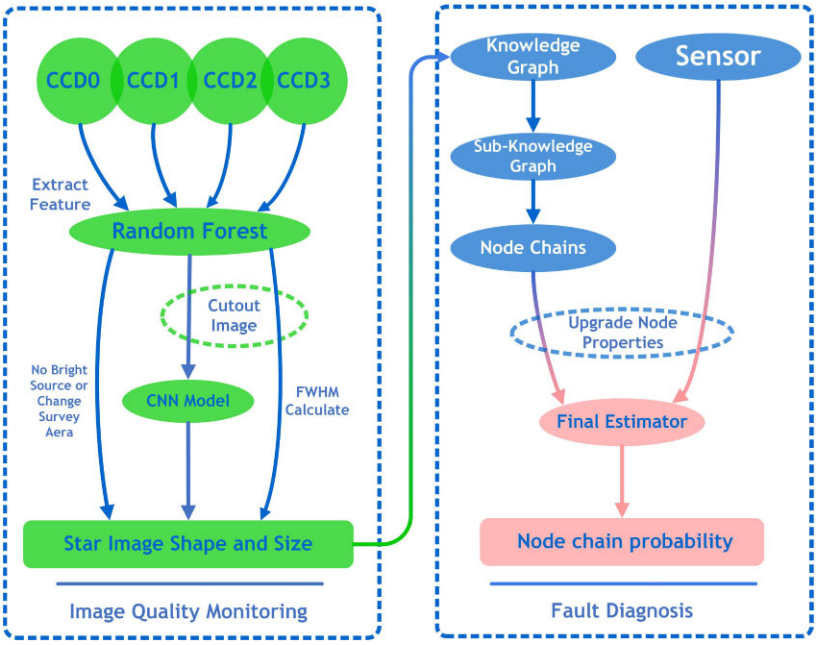

Figure 9. In the framework of the telescope maintenance support system, the left part realizes the imaging quality monitoring and the right part realizes the fault diagnosis.

as the multiplication of the probabilities of multiple actions being established. Thus the probability P_k of node chains k can be written in the form below,

$$P_k = \frac{e^{t_k/t_{\rm sum}}}{\sum_{l\in S} e^{t_l/t_{\rm sum}}} \prod_{i,j\in U\wedge(i\to j)} p_{ij}, \tag{2}$$

where S is the set of whole node chains, U is the set of node's ID of node chain k. And the p_{ij} is the established probability of action, which construct by two nodes i and j. This action represents a theorem if $p_{ij} = 1$ is always true. The t_k is times the node chains have caused poor imaging quality, and $t_{\rm sum}$ is the sum of times of this type of poor image quality in the history data.

KGs can give the possible node chains, and we can get the probability of the whole node chains and show the result to the maintainer based on the final estimator. The IQMDS's framework is demonstrated in Fig. 9.

4 RESULT AND DISCCUSION

We have provided the core concepts of our method. In this section, we exhibit the constructed details of the IQMDS based on LAMOST and use the idea of node importance in the KG to give the LAMOST devices that need priority attention in daily maintenance.

4.1 IQMS based on LAMOST

LAMOST uses a segmented mirror-reflected Schmidt optics system with an active Schmidt corrector. It includes a thin-mirror and segmented-mirror active optics reflecting Schmidt corrector (Ma) including 24 sub-mirrors, a segmented-mirror active optics spherical primary mirror (Mb) including 37 sub-mirrors, and a 1.75 m focal surface (Cui et al. 2012). One sub-mirror of Ma contains three displacement actuators, 34 force actuators and three fixed support. One sub-mirror of Mb has a three-displacement actuator.

We use the picture captured by the acquisition camera to monitor the image quality. Through the feature selection, the number of bright stars, correlation, and standard deviation of pictures are selected as input features of RF. The normal picture, according to the RF, is exported to the convolution neural networks, which divide the star images into five categories: circular, two-point-like, lumpy-like, donut-like, and stick-like images. Then the circular star image's full width at half-maximum is calculated. If the star image's shape is circular and full width at half-maximum exceeds 3.3 arcseconds, corresponding to the incidence angle of LAMOST fibre, the image quality is defined as the'big size star image'. Finally, if the classification result is abnormal, the result of the star image, which could be a lumpy-like shape star image, donut-like shape star image, stick-like shape star image, two-point-like shape star image, no bright star or big size star image, are exported to KRGS.

We have adopted the CNN architecture directly from our prior research. Comprehensive details regarding the CNN architecture and training procedures are available in reference (Hu et al. 2021). In Fig. 10, we again provide examples of star images with various shapes for training the CNN model. The 40 d observation data obtained by the acquisition camera in 2019 and 2020 is used to train the RF and CNN models. The classification accuracy can reach 96.7 per cent.

4.2 Knowledge graphs result generation system based on LAMOST

To construct the LAMOST KG, first, we use expert experience to arrange the LAMOST entities to a tuple form (head entity, relationship, and tail entity), with the elements meaning the subject, the predicate and the object, respectively. Then the entities and relationships are extracted from the logbook, which records the telescope fault and reason, to rich data. Entities and relationships are catalogued in separate entity and relationship files. The entity file

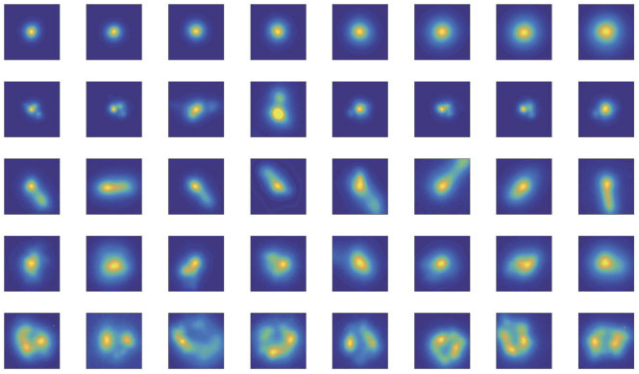

Figure 10. From top to bottom, the images represent different shapes of stars: normal star image, two-point star image, stick-like star image, lumpy-like star image, and donut-like star image. These star images serve as inputs for training the CNN.

encompasses the attributes of the entities, as detailed in Section 2.2. Conversely, the relationship file contains the IDs of the two nodes and the relationship between them. Finally, we use the KG construction software NEO4J to form the KG. In Table 1, we provide examples from the entity file.

The LAMOST image-quality-related KG describes the relationship of entities and contains 1295 nodes and 1300 relationships. Through the constructed KG, we use the cypher language to achieve three functions:

1. Match the input image quality to give a node chain pointing to this node;
2. Real-time update node parameters according to the received sensor data;
3. Calculate the importance of nodes in the KG.

A subgraph of the KG containing matching nodes is given for the input image quality. Fig. 11 shows examples of stick-like star images, and the KG subgraph was obtained by matching it with the constructed LAMOST KG. The result shows that nine node chains can lead to a stick-like image. The node chain indicates the cause of the poor imaging quality.

4.3 Final estimator and experiment based on simulation data

The traditional fault possibility estimator only considers the historical fault probabilities. This history-data-based method based on historical data uses the node chain with the highest historical fault probability as the diagnosis result, and the result of the estimator will not change in the short term. The result can be expressed as

$$P_k = \frac{t_k}{t_{\rm sum}}. \tag{3}$$

Our method combines the historical fault probabilities and the real-time high-frequency data from sensors to give the probability of each node chain. Based on node parameters, our method calculates the relationship's establishing probability p_{ij} between nodes i and j.

According to the preset parameter range of the telescope's normal and abnormal operation, p_{ij} is 0 or 1, when the parameters are within the normal set or abnormal set. The larger the difference dis_a between the value of the node parameter and the normal operation value range and the less the difference dis_b between the value of the node parameter and the abnormal operation value range, the greater the probability of the action being established. The p_{ij} can be written in the form below, and the detailed definition of dis_a and dis_b is shown in Fig. 12.

$$p_{ij} = \begin{cases} 0 & \text{value} \in \text{normal set} \\ \frac{dis_a}{dis_a + dis_b} & \text{value} \notin \text{range} \\ 1 & \text{value} \in \text{abnormal set.} \end{cases} \tag{4}$$

And now, some method based on the artificial neural networks method is used as an estimator. The FNN is the most common method. FNN (Sainath et al. 2015) consists of an input layer, output layer, and several hidden layers, each of which contains neurons that transmit information to the neurons in the next layer. The input data is transferred from the input layer and reaches the output layer, where the target variable is predicted.

Parameter $Par(k) = [\,a_k(1)\ a_k(2)\ \ldots\ a_k(n)\,]$ of node chains k construct a feature vector. The vector is imported to a fully connected neural network, which can give the established possibility of the node chain. To verify the effectiveness and advantages of our method, we compare the evaluation accuracy of the three approaches based on the simulation data. The stick-like image's final estimator with nine possible fault causes is constructed, and the simulation data contains the parameter and target. The name and value range of parameters is shown below:

(i) Wind speed v_w (0 to 10 m s^{-1}).
(ii) Wind direction $v_{\rm d}$ (0 to 360 degree).
(iii) Ma vertical angle $a_{\rm v}$ (32.3 to 77.3 degrees).
(iv) Ma azimuthal angle $a_{\rm a}$ (−20 to 20 degree).
(v) Step length of the Ma vertical angle rotating motor $l_{\rm v}a$ (0.01 to 1 arcsecond).
(vi) Step length of the Ma azimuthal angle rotating motor $l_{\rm a}a$ (0.01 to 1 arcsecond).
(vii) Step length of the focal surface rotating motor $l_{\rm r}$ (0.01 to 1 arcsecond).
(viii) Step length of the focal surface displacement motor $l_{\rm d}$ (0.01 to 1 arcsecond).
(ix) Step length of the focal surface alltitute motor 1 $l_{\rm a}1$ (0.01 to 1 arcsecond).
(x) Step length of the focal surface alltitute motor 2 $l_{\rm a}2$ (0.01 to 1 arcsecond).
(xi) Step length of the focal surface alltitute motor 3 $l_{\rm a}3$ (0.01 to 1 arcsecond).
(xii) Pressure of oil pad *pre* (0 to 300 V)

The wind pressure P of Ma sacrify

$$P = \frac{1}{2}\rho_{\rm air} V^2 A, \tag{5}$$

where the $\rho_{\rm air}$ is air mass density, V is wind velocity, and A is effective area of Ma exposed to wind. For the LAMOST, when the wind speed exceeds 5.5 m s^{-1} in the Ma mirror plane's normal direction, the deformation of the mirror surface seriously affects the image quality (Yang et al. 2005). At the same time, if the motor's steps and the oil pad voltage are not within the working range, the telescope will be faulty. Therefore, the parameter relationship of the

Table 1. The table showcases examples of four categories of entities employed in building the LAMOST KG: imaging quality, equipment, environment, and staff. The complete data set is accessible through the link provided in the data availability subsection.

ID	Class	Lable	Name	Special properties 1	Special properties 2
0	image quality	image quality	Stick like image	–	–
250	device	focal plane	focal attitude motor 01	step length	–
1280	enviroment	climatic conditions	site wind	wind speed	wind direction
1292	staff	staff	astronomor	operation	–

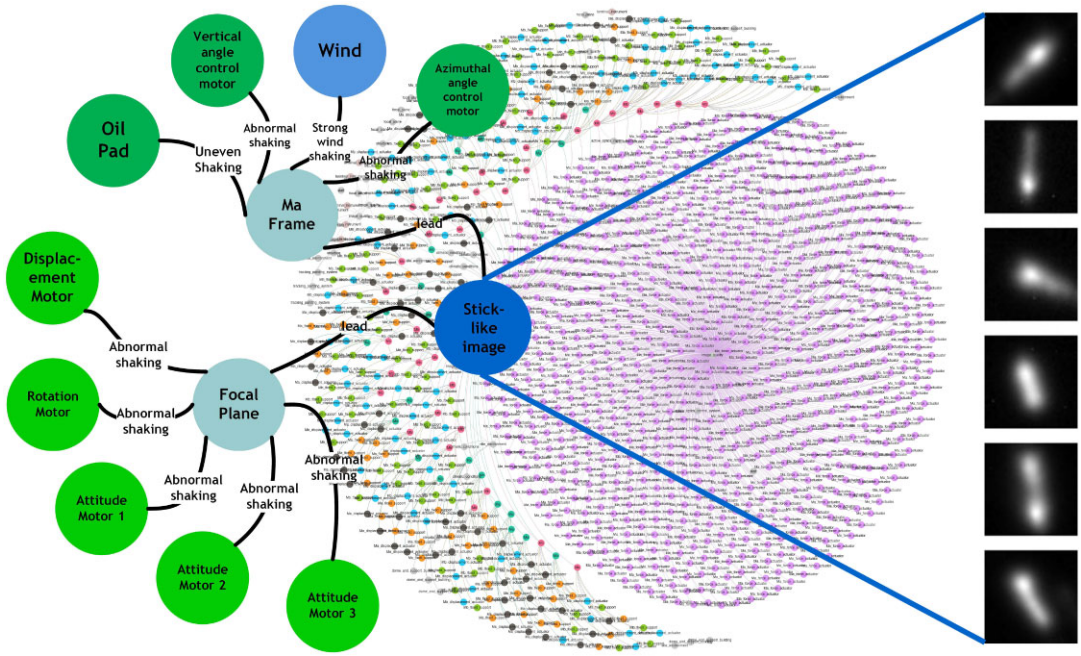

Figure 11. The right part is the stick-like star image; the middle part is constructed LAMOST KG; the left is the KG subgraph obtained by matching the'stick-like image' in the LAMOST KG-based query system.

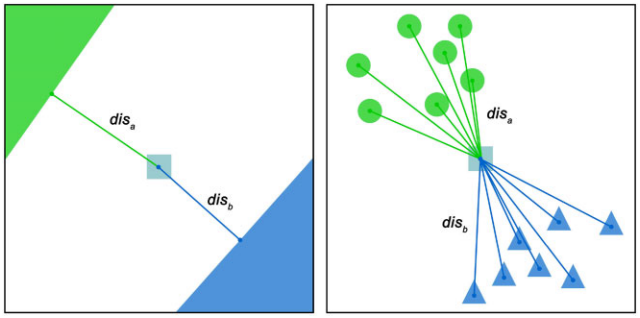

Figure 12. The square represents the parameter point of the action to be evaluated. The left subplot depicts a situation where the normal and abnormal data fall within a specific value range. In this context, dis_a signifies the Euclidean distance from the points to be evaluated to the nearest boundary point of the normal data set, while dis_b denotes the Euclidean distance from the points to be evaluated to the nearest boundary point of the abnormal data set. Conversely, the right subplot presents a scenario where the normal and abnormal data are represented as distinct points. Here, dis_a corresponds to the average Euclidean distance from the points to be evaluated to the points in the normal data set, and dis_b relates to the average Euclidean distance from the points to be evaluated to the points in the abnormal data set.

simulation data and the corresponding faults are shown below,

$$target = \begin{cases} a & v_w \cos(\text{angle}(\vec{v}_d, \vec{m}_a)) \geq 5.5 \\ b & l_v a \geq 0.1 \\ c & l_a a \geq 0.1 \\ d & l_r \geq 0.1 \\ e & l_d \geq 0.1 \\ f & l_a 1 \geq 0.1 \\ g & l_a 2 \geq 0.1 \\ h & l_a 3 \geq 0.1 \\ i & 240 \geq pre \parallel pre \geq 260. \end{cases} \quad (6)$$

Where a: heavy wind shake Ma frame; b: Ma vertical angle rotation motor abnormal shake cause Ma frame; c: Ma azimuthal angle rotation motor abnormal shake cause Ma frame; d: focal surface rotating motor abnormal shake focal surface; e: focal surface displacement motor abnormal shake focal surface; f: focal surface altitude motor 1 abnormal shake focal surface; g: focal surface altitude motor 2 abnormal shake focal surface; h: focal surface altitude motor 3 abnormal shake focal surface; i: uneven oil pad shake Ma frame.

The parameter's value is obtained by random sampling within the value range. We only consider the one-fault cause situation. Among the possible fault causes, the fault caused by the wind shaking Ma frame accounted for 36 per cent, and the fault caused by each other accounted for 8 per cent. 80 per cent of the data is used to calculate the historical fault probability and train the FNN. The remaining 20 per

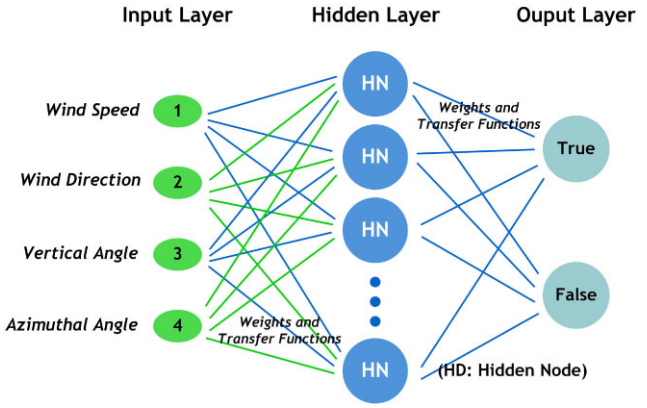

Figure 13. A FNN architecture related to the event where strong winds cause the Ma mount to sway, ultimately leading to the stick-like star images.

Table 2. The accuracy of the three methods. The result shows that our approach has similar accuracy to the FNN-based method and has higher accuracy than the history-data-based method. And FNN requires more data than our method to train parameters.

Method	Accuracy	Training data
History-data-based method	36.1 per cent	**small**
Our method	**92.8 per cent**	**small**
FNN-based method	**94.9 per cent**	large

cent of the data is used to calculate the prediction accuracy. Fig. 13 presents a FNN architecture related to the event where strong winds cause the Ma mount to sway, ultimately leading to the stick-like star images.

Using our method, we select the average values of parameters from abnormal data points in the simulated data set to establish reference points for calculating dis_b. Additionally, we determine reference points for calculating dis_a by using 20 per cent of the range of normal values from the simulated data. For example, the normal range for pressure is set between 248 and 252 V; the abnormal ranges would be defined as 0–120 V and 280–300 V.

The accuracy of the three methods is shown in Table 2. The result shows that our method has similar accuracy to the FNN-based method and has higher accuracy than the history-data-based method. A large amount of data and time need to train the FNN model, but telescopes usually work in normal conditions, which means limited fault data can be collected. Building machine learning models using a few machines' faulty samples is challenging to diagnose faults accurately. So we choose our method as the final estimator.

4.4 Experiment in LAMOST

The IQMDS is constructed based on LAMOST data. We count the logbook data from 2009 to 2022, and the cause of the fault is divided into 34. We calculated the probability of each fault cause, and the historical fault probabilities for various fault types are shown in Fig. 14. Given the lack of equipment parameters corresponding to the fault data, except for recent years, we determined the normal working range and abnormal working range of the entity's parameters through expert experience.

Constructed system is used to predict the cause of 20 faults from 2022 to 2023. The image quality and node parameters are found according to the fault time and imported into our system. The most possibility node chains are given. We represent the cause of the

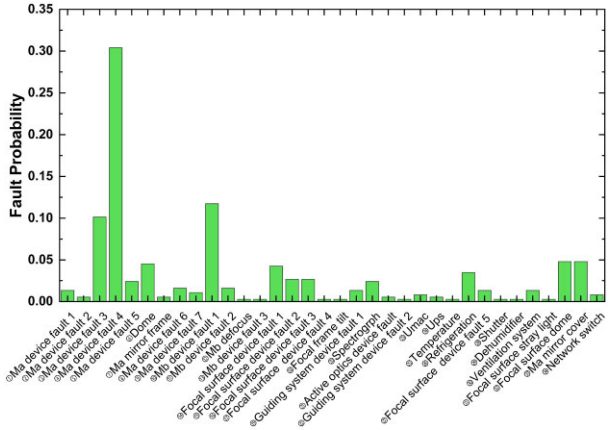

Figure 14. The distribution of history fault data is given, encompassing 34 distinct fault types. The most prevalent fault cause is 'Ma device fault 4".

Table 3. The comparison of the prediction result based on our system and the truth fault cause. The result of our prediction is a node chain, and the initial node of the node chain is taken as the predicted fault cause. The cause of the fault is represented by the numbers given in Fig. 14.

Image quality	Predict cause	Truth cause
lumpy-like	④	④
lumpy-like	④	④
two-point-like	③	③
two-point-like	⑩	⑩
two-point-like	⑩	⑩
lumpy-like	⑤	⑤
two-point-like	③	⑨
lumpy-like	⑤	⑤
two-point-like	⑩	⑩
two-point-like	⑩	⑩
stick-like	⑧	⑧
lumpy-like	④	④
two-point-like	⑩	⑩
lumpy-like	④	④
stick-like	⑧	⑧
stick-like	⑭	⑦ ⑭
No bright star	⑲	⑲
lumpy-like	④	④
No bright star	㉜	㉜
stick-like	⑦	⑦

fault as a node chain. In contrast, the fault cause documented in the maintenance log pertains to a specific entity's fault. This is synonymous with the initial node name within the node chain. To evaluate, we juxtapose the initial node from the node chain against the fault cause listed in the maintenance logbook. The comparative results are displayed in Table 3.

The results show that our system can diagnose faults with an accuracy of 90 per cent and can be used for telescope image quality monitoring and diagnosis.

4.5 Node importance

Node importance can guide the system to allocate limited resources for entities of high importance. The nodes that are most likely to

cause fault can be highlighted by calculating the importance of nodes, which helps to improve the maintenance efficiency for a new telescope which lacks the history data.

Referring to the PAGERANK algorithm (Haveliwala 2003), we give a method for calculating the importance of nodes. Assuming that the established probability of the action is the same, it is $1/n$, where n is the number of the relationship of the whole KG. The established likelihood of the path is $(1/n)^m$, where m is the number of actions in the path. The node importance is expressed as the sum of the probabilities of all paths that take it as the initial node and take the telescope imaging quality entity as the endpoint.

According to the above definition, we calculate the LAMOST KG node importance of different classes and find that: the most priority node of the device class is the submirror of Ma; the most priority node of the environment class is the atmosphere seeing.

5 CONCLUSIONS

The proposed telescope IQMDS aim at real-time monitoring and efficient diagnosis of the image quality. Our method uses star image shape and size to represent the telescope image quality, then gives the cause of poor image quality. Our proposed system can be divided into three components. First, an IQMS extracts the star image shape and size as telescope image quality. Secondly, a KRGS gives the possible cause of poor image quality. Thirdly, an estimator integrates the second component and sensor results to provide the final fault cause.

The 40 d observation data obtained by the acquisition camera in 2019 and 2020 are used to train the star image shape classification models. The classification accuracy can reach 96.7 per cent. The LAMOST image-quality-related KG is built up to describe the relationship of four classes of entities, which contains 1295 nodes and 1300 relationships. The final estimator is constructed based on the logbook data from 2009 to 2023 yr. Our system showed good performance in LAMOST.

The prospects for KGs more applications in the telescope are essential to discuss and achieve. For example, we can use the device brand as a device parameter to obtain more reliable products, use the structure of node chains to train the machine learning model, and then use the model to predict potential causes of the fault.

ACKNOWLEDGEMENTS

Thanks are given to the reviewer for the constructive comments and helpful suggestions. This work is supported by the National Nature Science Foundation of China (grant no U1931207, 12203079, 12103072, and 12073047), the Natural Science Foundation of Jiangsu Province (grant nos BK20221156 and BK20210988), and the Jiangsu Funding Program for Excellent Postdoctoral Talent (grant no 2022ZB448). The Guo Shou Jing Telescope (or LAMOST) is a National Major Scientific Project built by the Chinese Academy of Sciences. Funding for the project was provided by the National Development and Reform Commission. LAMOST is operated and managed by National Astronomical Observatories, Chinese Academy of Sciences.

DATA AVAILABILITY

The data underlying this article are available in KGs_System Repository at https://github.com/iphytian/KGs_System.

REFERENCES

Abbott B. et al., 2009, Rep. Prog. Phys., 72, 076901
Aksaker N., Yerli S. K., Erdoğan M., Kurt Z., Kaba K., Bayazit M., Yesilyaprak C., 2020, MNRAS, 493, 1204
Burrows C. J., Holtzman J. A., Faber S., Bely P. Y., Hasan H., Lynds C., Schroeder D., 1991, ApJ, 369, L21
Chen X., Jia S., Xiang Y., 2020, Expert Syst. Appl., 141, 112948
Cui X.-Q. et al., 2012, Res. Astron. Astrophys., 12, 1197
Deng L. et al., 2021, Nature, 596, 353
Gerb A., 1991, Telemat. Inform., 8, 283
Gómez S. L. S. et al., 2019, Publ. Astron. Soc. Pac., 131, 108012
Gunn J. E. et al., 2006, AJ, 131, 2332
Guo Q., Zhuang F., Qin C., Zhu H., Xie X., Xiong H., He Q., 2022, Proc. IEEE, 34, 3549
Haveliwala T. H., 2003, Proc. IEEE, 15, 784
Hogan A. et al., 2021, ACM Comput. Surv. (CSUR), 54, 1
Hu T. Z., Zhang Y., Cui X. Q., Zhang Q. Y., Li Y. P., Cao Z. H., Pan X. S., Fu Y., 2021, MNRAS, 500, 388
Landau R., 1994, Publ. Astron. Soc. Aust., 11, 180
Lawrence S., Giles C. L., Tsoi A. C., Back A. D., 1997, Proc. IEEE, 8, 98
Longo G., Merényi E., Tiňo P., 2019, Publ. Astron. Soc. Pac., 131, 1
Manola F., Miller E., McBride B. et al., 2004, W3C recommendation, 10, 6
McGehee P. M. et al., 2002, in Lewis H., ed., Proc. SPIE Conf. Ser. Vol. 4848, Advanced Telescope and Instrumentation Control Software II. SPIE, Bellingham, p. 156
Mukund N., Thakur S., Abraham S., Aniyan A., Mitra S., Philip N. S., Vaghmare K., Acharjya D., 2018, ApJS, 235, 22
Nelson J. E., Mast T. S., Faber S. M., 1985, Keck Observatory Report
Sainath T. N., Vinyals O., Senior A., Sak H., 2015, in 2015 IEEE international conference on acoustics, speech and signal processing (ICASSP). South Brisbane, QLD, Australia, p. 4580
Shanks T. et al., 2015, MNRAS, 451, 4238
Singhal A., 2012, Official google blog, 5, 16
Stobie R., Meiring J. G., Buckley D. A., 2000, in Dierickx P., ed., Proc. SPIE Conf. Ser. Vol. 4003, Optical Design, Materials, Fabrication, and Maintenance. SPIE, Bellingham, p. 355
Tamai R., Spyromilio J., 2014, in Stepp L. M., Gilmozzi R., Hall H. J., eds, Proc. SPIE Conf. Ser. Vol. 9145, Ground-based and Airborne Telescopes V. SPIE, Bellingham, p. 914501
Teimoorinia H., Kavelaars J., Gwyn S., Durand D., Rolston K., Ouellette A., 2020, AJ, 159, 170
Tissot H. C., Pedebos L. A., 2021, J. Healthc. Inform. Res., 5, 1
Xie L., Hu Z., Cai X., Zhang W., Chen J., 2021, Complex and Intell. Syst., 7, 1241
Xu J. et al., 2020, Sci. data, 7, 1
Yang D., Chen K., Liang Y., Cui X., 2005, in Hatheway A. E., ed., Proc. SPIE Conf. Ser. Vol. 5877, Optomechanics 2005. SPIE, Bellingham, p. 307
Zhao G., Zhao Y.-H., Chu Y.-Q., Jing Y.-P., Deng L.-C., 2012, Res. Astron. Astrophys., 12, 723
Zheng Z.-P., Qiu B., Luo A.-L., Li Y.-B., 2020, Publ. Astron. Soc. Pac., 132, 024504
Zou X., 2020, in J. Phys.: Conference Series, 1487, 012016

This paper has been typeset from a TEX/LATEX file prepared by the author.